RSC Advances

PAPER

Cite this: *RSC Adv.*, 2015, **5**, 34652

Photocatalytic oxidative desulfurization of dibenzothiophene by C/TiO_2@MCM-41 nanoparticles under visible light and mild conditions

Mahshid Zarrabi,[a] Mohammad H. Entezari*[ab] and Elaheh K. Goharshadi[c]

Today, due to the environmental pressures on the sulfur content of gasoline and fuel cell applications, refineries need a very deep desulfurization process to reach the ultra-low sulfur diesel (ULSD, 1 ppm). In this research, dibenzothiophene (DBT) in *n*-octane solution (as a diesel fuel model) was completely converted into biphenyl by visible light irradiation in the presence of C/TiO_2@MCM-41 (CTM-41) as a photocatalyst under mild conditions. For the first time, the conversion was carried out through oxidation in one phase without using oxidant. For synthesizing CTM-41, tetra-butylorthotitanate was used as a precursor of Ti. Carbon species were identified in CTM-41 by X-ray photoelectron spectroscopy and UV-Vis spectroscopy. The self-doped carbon in CTM-41 was attributed to the tetra-butylorthotitanate used as a precursor of Ti. In the synthesis process, there was no carbon precursor addition. The formation of two types of carbon (carbonate species and coke-like structure in lattice of TiO_2) is responsible for the visible photocatalytic activity of the catalyst. The samples were characterized by X-ray diffraction, FTIR and UV-Vis spectroscopy. The specific surface areas of the prepared catalysts determined by the nitrogen adsorption–desorption isotherm at 77 K were 922.42 m^2 g^{-1} and 767.54 m^2 g^{-1}. The GC-MS analysis confirmed the conversion of DBT to biphenyl. Based on the experimental results, the hole and hydroxyl radical as reactive species in the proposed mechanism played the key roles in the photocatalytic desulfurization process.

Received 9th February 2015
Accepted 9th April 2015

DOI: 10.1039/c5ra02513c

www.rsc.org/advances

1. Introduction

Ultra deep desulfurization of fuels has attracted a great deal of attention. This is not only for legislation enforcing environmentally friendly transportation fuel but also the severe requirement of liquid hydrocarbon fuels with sulfur content of less than 1 ppmw for fuel cell applications.[1,2] Currently, the sulfur removal from various liquid hydrocarbon streams is conducted by the catalytic hydrodesulfurization (HDS) process at 300–400 °C and 3–6 MPa hydrogen pressure with high hydrogen consumption in refineries. Although HDS process is a conventional technology for desulfurization of liquid fuels, it cannot efficiently eliminate refractory compounds such as alkylthiophenes, benzothiophene (BT), dibenzothiophene (DBT), and its derivatives.[1,3–5] Oxidative desulfurization (ODS) is considered to be one of the promising new methods for deep desulfurization of fuels. The photocatalytic ODS is attracting interest, because of its low cost and mild operation of conditions.[6–10]

Photocatalysis has emerged as a promising technology for the degradation of organic pollutants. TiO_2 is the most widely used photocatalyst in various applications due to its high photocatalytic activity, lower cost, nontoxic nature, chemical inertness, and simplicity but it has some disadvantages.[1,11–13] However, TiO_2 can agglomerate very easily during the synthesis process which has adverse effects on the catalytic efficiency. In addition, in the bare TiO_2 nanoparticles a rapid recombination can be occurred for the photogenerated electron–hole pairs. These disadvantages limit wide spread use of the TiO_2 for various applications. Uniform ordered channels of mesoporous materials such as MCM-41 can control the particle size of TiO_2 and efficiently prevent particles from agglomeration.

In general, the photocatalytic activity of TiO_2@MCM-41 is higher than TiO_2. This is due to long-lived photo induced charge separation, large pore size, and high specific surface of MCM-41 which has the ability to adsorb some bulky reactants. The introduction of transition metals into MCM-41 increases the active sites of the photocatalyst.[14–16]

[a]*Sonochemical Research Center, Department of Chemistry, Faculty of Science, Ferdowsi University of Mashhad, 91775, Mashhad, Iran. E-mail: moh_entezari@yahoo.com*

[b]*Environmental Research Center, Department of Chemistry, Faculty of Science, Ferdowsi University of Mashhad, 91775, Mashhad, Iran*

[c]*Nano Research Center, Department of Chemistry, Faculty of Science, Ferdowsi University of Mashhad, 91775, Mashhad, Iran*

Another disadvantage of TiO_2 is exhibiting low efficiency under visible light because it has large band gap energy of 3.2 eV, corresponding to a threshold wavelength of 388 nm. Much study was performed by UV light irradiation because TiO_2 can only absorb UV light. In general the photocatalysts with narrow band gaps are suitable for desulfurization under visible light irradiation.

The doping of nonmetallic elements has been regarded as a promising strategy for improving visible light activity of TiO_2-based photocatalysts.[17,18] Among such elements, carbon, sulfur, and nitrogen atoms have been shown to effectively enhance the visible light activity of TiO_2. These nonmetallic atoms can substitute in the lattice structure of TiO_2 causing substantial improvements in the visible light activity as compared to that of pure TiO_2.[19–21]

In this work, dibenzothiophene was successfully degraded at low temperature and atmospheric pressure by CTM-41 under visible light irradiation. For the first time, the photocatalytic degradation was carried out without adding an oxidant. It was confirmed that the presence of carbon in the synthesized photocatalyst has a major role in the degradation. In addition, a mechanism was proposed for the degradation of DBT.

2. Experimental

2.1. Materials

Tetra-butylorthotitanate (98%), ethanol (99.5%), dimethyl sulfoxide (DMSO, 99%), ammonium oxalate (AO, 99.5%) and hexane were supplied by Merck. Dibenzothiophene (DBT), titanium tetrachloride ($TiCl_4$, 99.9%) and *p*-benzoquinone (BQ) from Sigma-Aldrich, *n*-octane (95%) from Samchun, MCM-41 from Gas Chemical Company of China, and de-ionized water were used for washing and sample preparation.

2.2. Preparation of the catalyst

2.2.1. TBOT as a precursor. The CTM-41 composites with two different molar ratios of Si/Ti (5, 50) were synthesized. The amount of 1.5 g of calcined MCM-41 was placed in a 100 mL round-bottom flask with 50 mL of dried hexane.

The mixture was stirred for 30 min at room temperature. Then, a certain amount of TBOT was added. The mixture was stirred and refluxed at 343 K for 20 h under nitrogen atmosphere. The solid was separated from the mixture using centrifugation at rate of 5000 rpm. The product was washed four times with dry ethanol. The solid was then hydrolyzed in a beaker with 150 mL of deionized water. The mixture was stirred for another 4 h. Then, the product was washed with deionized water, centrifuged at rate of 5000 rpm, and finally air dried at 373 K. The white powder as modified sample was obtained after calcination at 773 K for 2 h.[22]

2.2.2. Titanium tetrachloride as a precursor. The catalyst was synthesized by the same previous procedure but, $TiCl_4$ was used instead of TBOT as Ti precursor.

2.3. Characterization techniques

The X-ray diffraction (XRD) patterns (2θ = 10–80°) were recorded by Bruker-AXS, D8 Advance model at a scanning rate of 0.04° s^{-1}. The wide angle and small angle X-ray diffraction were performed with monochromatized Cu-Kα radiation (λ = 1.5406 Å) and Co-Kα radiation (λ = 1.7890 Å), respectively. The Fourier-transformed infrared spectra (FT-IR, Avatar 370) using the KBr pellet method was recorded on a Thermo-Nicolet spectrometer. The optical absorption spectrum of the DBT was measured using UV-Vis spectroscopy (Unico 2800). The X-ray photoelectron spectroscopy (XPS) was performed using an ESCA PHI 5000 instrument and Al-Kα irradiation (1486.6 eV) to determine the chemical states of Ti, S, O, and C atoms in the prepared samples. The N_2 adsorption isotherms of samples were measured at 77 K on a Bel Japan apparatus (Belsorp mini II model) to calculate BET specific surface areas, pore volumes, and pore sizes of the powder samples. The structural of the samples were determined with transmission electron microscope (TEM, Philips CM-120). The GC (Agilent 6890N) and MS (Agilent 5975B) were also used for the determination of the by products produced during the degradation process.

2.4. Photocatalytic degradation of DBT

The degradation was performed under constant stirring in a 50 mL glass vessel containing 10 mL of *n*-octane solution of DBT (300 ppm) as a fuel model and 0.015 g CTM-41 as a catalyst. Before illumination, the suspension was magnetically stirred for 45 min to attain adsorption–desorption equilibrium between photocatalyst and DBT in the dark. It was then illuminated with two 300 W tungsten lamps (visible irradiation) at 333 K for 5 h. The absorption of DBT was monitored with a UV-Vis spectrophotometer at λ_{max} = 325 nm. The strong absorbance at 325 nm suggests an n–π^* excitation similar to that for the sulfur atom in DBT.[23] The absorption was converted to the concentration through the standard curve. The degradation of DBT was calculated according to the initial and final concentration of DBT in the solution:

$$x = \left(\frac{C_0 - C}{C_0}\right) \times 100$$

where x is the percent of degradation, C_0 and C (mg L^{-1}) stand for the initial and final concentration of DBT, respectively. For approving the degradation of DBT, the liquid phase was separated from the catalyst by centrifuging. Then, the organic phase and catalyst were extracted for GC-MS analyses.

3. Results and discussion

3.1. Characterization of the catalyst

3.1.1. FT-IR spectra. Fig. 1 shows the FT-IR spectra of calcined MCM-41 and CTM-41 with two different precursors. The bands at 1084.78 cm^{-1} and 810.84 cm^{-1} assigned to the asymmetric and symmetric stretching vibrations of framework Si–O–Si, respectively. The stretching vibration of the Si–O–Ti appears at about 956 cm^{-1} and enhances with decreasing Si/Ti molar ratio.[24]

3.1.2. Nitrogen adsorption–desorption. The N_2 adsorption–desorption isotherms of MCM-41 and CTM-41 samples are illustrated in Fig. 2. Some differences were observed between the nitrogen sorption curves of doped and undoped titania

samples. The isotherms for samples are apparently of type IV, typical of mesoporous materials.

The first adsorption at low pressure ($P/P^\circ < 0.01$) was caused by monolayer adsorption of N_2 on the walls of the mesopores. Upon monolayer adsorption, multilayer of nitrogen starts to develop at higher relative pressure of nitrogen (P/P° = 0.01–0.34). At relative pressure between 0.34 and 0.40, a sharp inflection due to capillary condensation with mesopores is observed. The sharpness of the step indicates a uniform pore size distribution. The sharpness of the step diminishes with titania loading which implies that the highly mesoporous structure was decreased but the structural regularity is not significantly affected. A summary of results obtained from N_2 adsorption–desorption isotherms of MCM-41 and CTM-41 with two different Si/Ti molar ratios are given in Table 1. The increase of the metal content leads to a gradual reduction in pore volume and total surface area. It may be due to the formation of large TiO_2 nanoparticles but decreasing of titanium incorporated in the pore wall (Si–O–Ti) from CTM-41 (Si/Ti = 50) to CTM-41 (Si/Ti = 5) causes the increasing pore diameter from CTM-41 (Si/Ti = 50) to CTM-41 (Si/Ti = 5).

3.1.3. XRD patterns

3.1.3.1. Small angles. The small angle XRD (SAXRD) profiles of MCM-41 and CTM-41 with two different Ti loadings are presented in Fig. 3. It is shown that MCM-41 pattern has a strong peak at $2\theta = 2.55^\circ$ and two weak peaks at $2\theta = 4.43^\circ$, 5.13° assignable to the crystallographic planes of (100), (110), and (200), respectively. This pattern proves the high order of the pores in the MCM-41 mesoporous structure.

The SAXRD data, wall thickness (W), unit cell parameter (a_0), and micro-strain (ε) are listed in Table 2. When the Ti content increased, a decrease in the intensity of the main diffraction peak (100 peak) was observed. This is due to the scattering contrast decreases between the pores and pore walls. The CTM-41 samples show strong d_{100} reflection peak which suggests a well order nanostructure of MCM-41 which was retained even after the loading of titania. As the Ti content increased, a small shift in the position of main peak to the higher angles was observed. This is due to the contraction of mesoporous framework which may be correlated with the calcination of samples. Therefore, the interplanar distance (d_{100}) and the hexagonal unit cell parameter (a_0) of the samples decreased with increasing of Ti content in the samples. The wall thickness (W) of the hexagonal arranged pore was calculated from $W = a_0 - D$. The results showed that the increase of wall thickness in CTM-41 (0.02) can be attributed to the Ti incorporation in the wall of the pore but the decrease of wall thickness in CTM-41 (0.2) may be correlated to the crystalline titania which was not incorporated in the wall. The broadening of XRD peaks ($\Delta\beta = 0.03^\circ$) are observed for Ti doped CTM-41 (0.02). The small changes in the broadening of the peak can be due to the increase of micro-strain. The small changes are attributed to the incorporation of Ti into the Si–OH bands on the surface of the pore. The FWHM (β) value of CTM-41 (0.2) shows the inverse trend which indicates formation of TiO_2 (anatase) phase. The micro-strain (ε) was calculated according to the formula of micro-strain which is: $\varepsilon = (\beta \cos \theta)/4$.

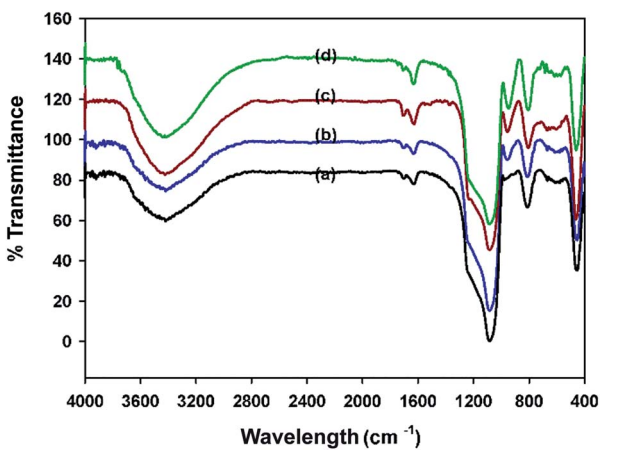

Fig. 1 FT-IR spectra: (a) MCM-41, (b) CTM-41 (Si/Ti = 50, TBOT), (c) CTM-41 (Si/Ti = 5, TBOT), (d) CTM-41 (Si/Ti = 5, $TiCl_4$).

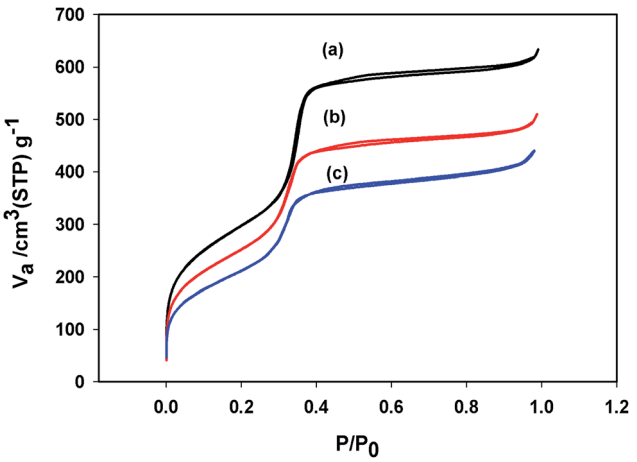

Fig. 2 Nitrogen adsorption–desorption isotherms of (a) MCM-41, (b) CTM-41 (Si/Ti = 50), (c) CTM-41 (Si/Ti = 5).

3.1.3.2. Large angles. Fig. 4 shows the wide angle X-ray diffraction patterns. The XRD pattern of the pure MCM-41 shows a broad peak between $2\theta = 15^\circ$ and 30° which confirms the amorphous silica structure.[25] After incorporating of TiO_2 into the MCM-41, a decrease in the intensity of the maximum peak was observed. The existence of broad peak indicates that the composites are still amorphous. There are no XRD peaks for

Table 1 Textural properties of MCM-41 and CTM-41 with different TiO_2 contents[a]

	D (nm)	S_{BET} ($m^2\ g^{-1}$)	V_T ($cm^3\ g^{-1}$)
MCM-41	3.63	1076.50	0.98
CTM-41 (Si/Ti = 50)	3.42	922.42	0.79
CTM-41 (Si/Ti = 5)	3.55	767.54	0.68

[a] D (nm): average pore diameter, S_{BET} ($m^2\ g^{-1}$): surface area, V ($cm^3\ g^{-1}$): total pore volume.

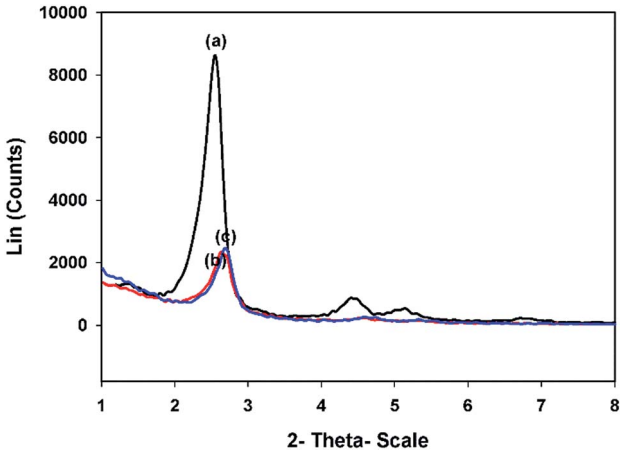

Fig. 3 SAXRD patterns of (a) MCM-41, (b) CTM-41 (Si/Ti = 50), (c) CTM-41 (Si/Ti = 5).

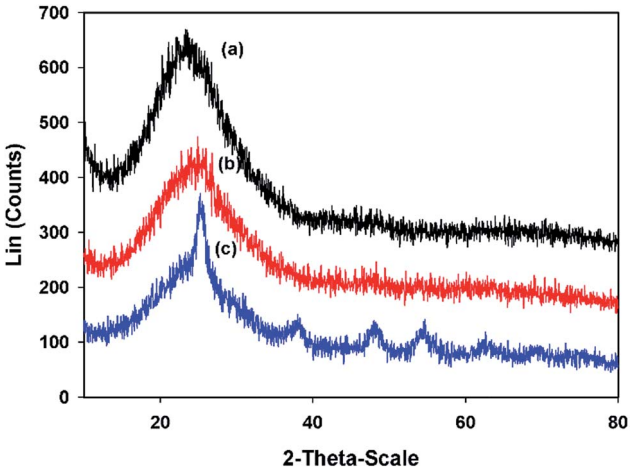

Fig. 4 XRD wide-angle patterns of (a) MCM-41, (b) CTM-41 (Si/Ti = 5), (c) CTM-41 (Si/Ti = 50).

the TiO_2 in the CTM-41 (Si/Ti = 50) composite which are related to the condensation of Ti with pendant Si–OH groups on the pore surface and generating tetrahedral Ti species instead of TiO_2 as a secondary phase segregation. In addition, the sizes of formed TiO_2 may be very small to detect. Meanwhile, for CTM-41 (Si/Ti = 5), additional peaks were appeared at 2θ = 25.3240, 37.9860, 48.0520, 54.7630, and 62.6760. These peaks are attributed to the presence of anatase phase of TiO_2 as secondary phase segregation. The average crystal size of the anatase phase for CTM-41 (Si/Ti = 5) was determined by the Scherrer formula and it was 6.89 nm. The emergence of new peaks in the wide angle and the inverse trend of the FWHM value for CTM-41 (Si/Ti = 5) are reasons for entity anatase phase. The shift of position of the maximum intensity to a higher value is probably resulted from the slight structural change as the micro-strain increases.

3.1.4. TEM analysis. Fig. 5 shows the TEM image of CTM-41 (Si/Ti = 5). It shows the parallel orientation of channels.

The long and straight mesopores of MCM-41 support is conserved and unaffected by the presence of titania.

3.1.5. XPS analysis. The XPS analysis of CTM-41 (Si/Ti = 5) was carried out in order to find the composition of the surface. Fig. 6 Shows the XPS spectrum of this sample. It mainly contains Ti, Si, O, C. The binding energies of C 1s, Ti 2p, O 1s, and Si 2p are located at 284.8 eV, 461.3 eV, 533.1 eV, and 105.4 eV, respectively.

Table 2 Pore structure parameters of MCM-41 and composites with different TiO_2 contents[a]

	2θ (°)	d_{100} (nm)	a_0 (nm)	W (nm)	FWHM (β)	ε (10^{-3})
MCM-41	2.55	4.110	4.640	1.007	0.287	1.249
CTM-41 (50)	2.63	3.949	4.508	1.090	0.290	1.265
CTM-41 (5)	2.67	3.877	4.434	0.886	0.272	1.181

[a] d_{100} (nm): interplanar distance, a_0 (nm): hexagonal unit cell parameter, calculated from $a_0 = 2d_{100}/3^{1/2}$, W (nm): wall thickness, calculated using $W = a_0 - D$.

Fig. 7 shows the XPS peaks of the carbon-doped in the composite. This is due to the diffusion of the carbon atoms during the synthesis process. Alkoxide residues after hydrolysis may result in carbon entering. Therefore, it was suggested that the peak at 283.7 eV is originated from Ti–alkoxide derived C–C species which is different from adventitious carbon species. These carbon residues may form highly condense and coke-like structure around TiO_2 nanoparticles and play the role of a sensitizer like organic dye molecules.[26]

A peak around 281 eV resulting from Ti–C bond is not observed, so carbon is not substituted by oxygen atom in the anatase lattice.[31]

Other two peaks around 286 and 288 eV are attributed to C–O and C=O, respectively which show the incorporation of carbon atoms into the interstitial positions of the TiO_2 lattice. The formation of carbonate ions or carbon atoms into the lattice of TiO_2 can be occurred by replacing titanium atoms in the form of Ti–O–C.[27–30] A peak around 281 eV resulting from Ti–C bond is not observed, so carbon is not substituted by oxygen atom in the anatase lattice.[31]

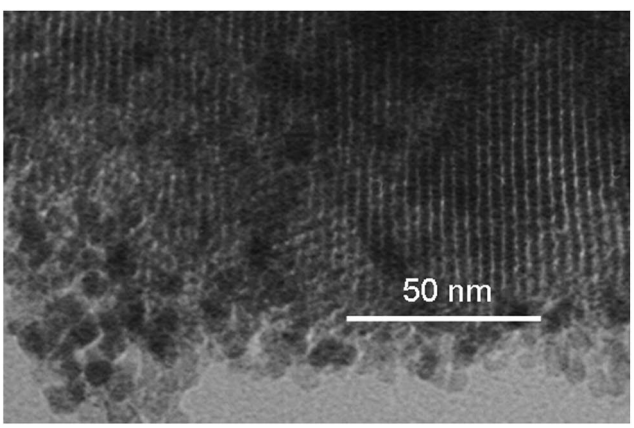

Fig. 5 TEM image and the selected-area diffraction patterns of CTM-41 (Si/Ti = 5).

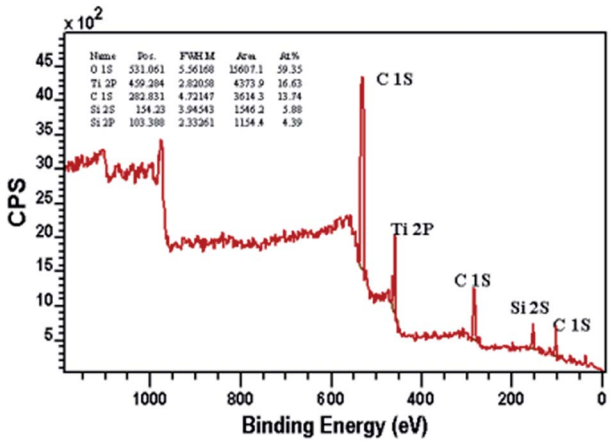

Fig. 6 The XPS survey spectrum of CTM-41 (Si/Ti = 5).

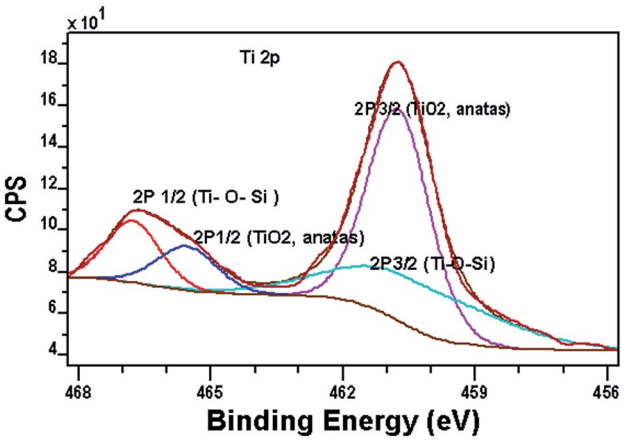

Fig. 8 The XPS spectrum of the Ti 2p.

Fig. 8 shows the XPS spectrum of Ti 2p region. The Ti 2p signals split into two peaks, which attributed to the Ti $2p_{3/2}$/Ti $2p_{1/2}$ binding energy region. The peak Ti $p_{3/2}$/Ti $2p_{1/2}$ for TiO_2 in the CTM-41 sample appears at 460.3/465.5 eV. In comparison to the binding energy of TiO_2 anatase (458.8/464.5 eV),[25,32] there is a slight red-shift about (1.5/1 eV) for TiO_2 in the CTM-41 sample. This shows that Ti^{3+} species are formed in the carbon-doped titania which indicates presence of carbonate ions because of interstitial doping of carbon in lattice.[16,27,33] The peak at 460.7/466.7 eV is consistent with silica, where cross-linking Ti–O–Si bonds. The O 1s spectra are shown in Fig. 9. The low binding energy near 530 eV is ascribed to anatase (Ti–O–Ti). The band near 532.2 eV is due to Si–O–Ti and terminal TiOH. The peak at 534.9 eV is attributed to SiO_2, H_2O and bridged TiOH. The binding energy at 536.2 eV is assigned to be Si–OH. The XPS results for the grafted sample CTM-41 (Si/Ti = 5) are summarized in Table 3.

3.1.6. UV-Vis analysis. The UV-Vis spectrum of the sample (Si/Ti = 5, 50) is shown in Fig. 10. The CTM-41 samples exhibit absorption in the visible range from 400 to 800 nm. The band gap energy was calculated by using Tauc's equation. The inset figures show the plot of $(\alpha h\nu)^{1/2}$ *versus* $h\nu$ (eV) for CTM-41 samples. The corresponding band gaps were about 1.3 and 3.2 eV by extrapolating the linear portion of $(\alpha h\nu)^{1/2}$ against $h\nu$ to point $\alpha = 0$.[34]

Palanivelu *et al.* reported that the band gap narrowing is due to the carbon impurity states which are attributed to substitutional C atoms replacing O atoms (Ti–C bonds) or interstitial C atoms (carbonate ions).[27,35–38] As the XPS spectra show, carbon is not substituted by oxygen atom in the lattice of anatase (absent of Ti–C bonds at 281 eV); therefore, the band gap narrowing for the CTM-41 can be explained by the isolated C 2p states of ions in the band gap of TiO_2.[12,37] Then, the carbonate values of 1.3 eV and 3.2 eV represent the band gap energies of the C/TiO_2 between valence and interbands and between the valence and conduction bands, respectively.[39–41] Previous reports show that the formation of carbonate species could cause an obvious long-tail absorption in the visible region.[42,43] Therefore, existence of long-tail absorption in UV-Vis spectrum of the samples also confirms the presence of carbonate ions.[43]

Further analysis of the UV-Vis absorption spectrum indicates that CTM-41 (Si/Ti = 5) has a stronger visible light absorption from 410 to 600 nm than that of observed for CTM-41 (Si/Ti = 50). On the other hand, the visible light absorption is improved with the increase of carbon content (see Table 4).

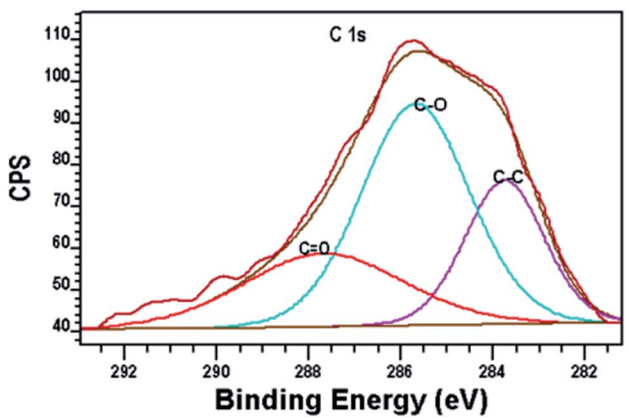

Fig. 7 The XPS spectrum of the C.

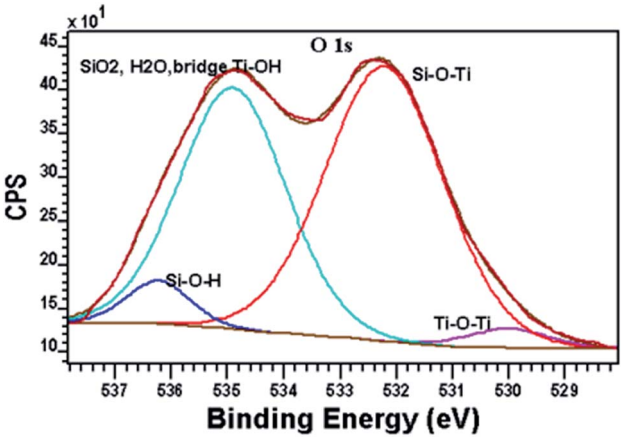

Fig. 9 The XPS spectrum of the O 1s.

Table 3 Binding energies and atomic concentrations from the X-ray photoelectron spectra of CTM-41 (Si/Ti = 5)

Element/orbital	Binding energy (eV)	Atomic content (%)	Assignment
Si 2p	105.4	9.73	SiO_2
Si 2s	156.2	13.1	
O 1s	530.0	0.83	TiO_2
	532.2	17.43	Si–O–Ti
	534.9	13.76	SiO_2, (TiOH)
	536.2	1.48	Si–OH
Ti $2p_{3/2}$/Ti $2p_{1/2}$	460.7/466.7	12.02	Ti–O–Si
	460.3/465.5	7.64	TiO_2 (anatase)
C 1s	283.7	5.83	O–Ti–C
	285.7	12.2	(C=C, C–C)
	287.6	5.97	CO_3^{2-}

3.2. Mechanism of carbon formation in CTM-41

Based on the XPS analysis of CTM-41, the peak at 283.7 eV shows the alkoxide residues after hydrolysis. Therefore, it is suggested that $Ti(OC_4H_9)_4$ is hydrolyzed by H_2O. Butyl alcohol (BuOH) and $Ti(OH)_4$ were formed. Then, dibutyltitanate was decomposed by calcination at 500 °C (Fig. 11).[44] Furthermore, in order to confirm that TBOT acts as a precursor of carbon, the CHN elemental analysis on CTM-41 samples with $TiCl_4$ and TBOT as precursors were performed. The CTM-41 samples were synthesized with $TiCl_4$ and TBOT as precursors by the similar procedure (see Section 2.2.1 and 2.2.2).

Table 4 shows that the catalyst prepared by $TiCl_4$ contains 0.08% carbon, while the sample prepared by TBOT contains 0.53% and 1.8% carbon in the catalyst with the ratio of Si/Ti = 50 and Si/Ti = 5, respectively.

The results indicate that carbon can be self-doped when butyl alcohol (BuOH) is formed by the hydrolysis of titanium dibutyltitanate and decomposition by calcination.

3.3. Photocatalytic degradation of DBT by CTM-41

The catalytic performance of CTM-41 was investigated in dark and under visible irradiation with two ratios of Ti loading (Fig. 12).

With increasing Ti loading, the removal of DBT was increased in dark and light too. The removal of DBT in dark was proceeded *via* adsorption which is attributed to the mesoporosity of CTM-41 and Lewis acid sites of tetrahedral Ti species in the framework of the catalyst. Increasing Ti loading leads to an increase in acid sites.[15,37,45] As shown in Fig. 12, the removal of DBT was 53.9% by the catalyst with lower ratio (Si/Ti = 5) and 44.7% with higher ratio (Si/Ti = 50) in dark. These results represent that the Lewis acid sites of tetrahedral Ti species for the adsorption are more important than pore volume and surface area of the catalyst. The removal of DBT under visible light can be proceeded in the presence of the carbon.

In other words, the degradation of dibenzothiophene depends on the amount of carbon and Si/Ti ratio. The amount of carbon was also increased with the ratio of Si/Ti (see Table 4).

3.4. Photocatalytic desulfurization mechanism

Some experiments were designed to elucidate the degradation mechanism. At first, one experiment was carried out in DBT solution without photocatalyst. The results showed that the absorption does not change with increasing the irradiation time. It means that DBT is stable in the presence of light in the absence of photocatalyst.

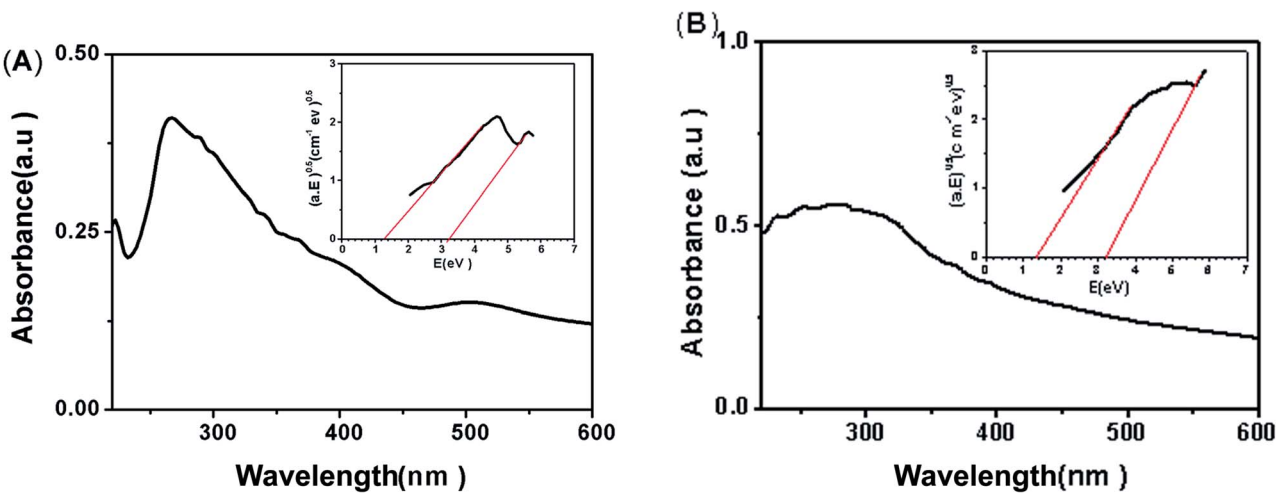

Fig. 10 Absorption spectra and Tauc's plots for obtaining the band gap (A) CTM-41 (Si/Ti = 50), (B) CTM-41 (Si/Ti = 5).

Table 4 The CHN elemental analysis of the catalysts

Sample	% C	% H
CTM-41 with $TiCl_4$ precursor (5)	0.08	0.60
CTM-41 with TBOT precursor (5)	1.80	0.88
CTM-41 with TBOT precursor (50)	0.53	0.65

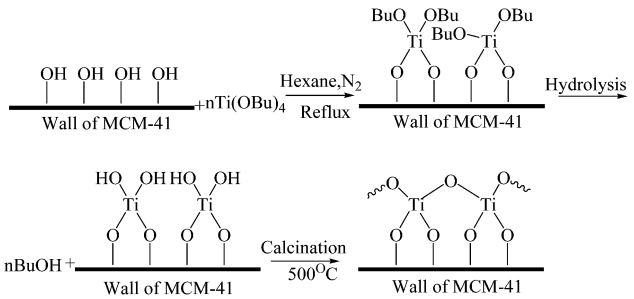

Fig. 11 Schematic reaction between MCM-41 and TBOT.

Also, some experiments were performed using different radical scavengers[39]

As shown in Fig. 13, when the dimethyl sulfoxide (DMSO) was added as a scavenger for hydroxyl radicals, desulfurization of DBT was remarkably inhibited (reduced from 95.6% to 12.7%).

This behaviour was attributed to the reaction of DMSO with hydroxyl radicals and reducing its concentration. When *p*-benzoquinone (BQ) was added for the superoxide anion *radicals*, desulfurization of DBT was reduced from 95.6% to 77.6%. This implies that the superoxide anion *radicals* ($O_2^{-\bullet}$) play minor roles in the degradation of DBT.

Also, the usage of inert N_2-saturated atmosphere causes a low desulfurization. Addition of ammonium oxalate (AO) as a scavenger for holes reduced desulfurization from 95.6% to 52.7%. Therefore, hydroxyl radicals ($OH^{\bullet}$) and holes (h^+) are the primary oxidants in our photocatalytic oxidation. The energy diagram for CTM-41 presents the proposed mechanism. This is based on the formation of impurity level (C 2p level of isolated carbonate ions) above the valence band of TiO_2 and the role of photosensitizer of coke-like species.

Under visible light irradiation, the electrons excitation from the valence to impurity level (C 2p level) and from impurity level to conduction band led to the generation of electron–hole pairs. The coke-like species also play the role of photosensitizer (P) like organic dyes which can be excited and injected electrons into the conduction band of TiO_2. Then, the rate of electron transfer to the adsorbed oxygen onto surface of TiO_2 nanoparticles increased. The electrons can be trapped by the isolated tetrahedrally coordinated Ti-oxide species (Ti^{4+}) dispersed in MCM-41 to generate Ti^{3+} ion. In the presence of O_2, the Ti^{3+} sites easily react with O_2 and form $O_2^{-\bullet}$.[36]

$$e^- + Ti^{4+}OH \rightarrow Ti^{3+}OH$$

$$Ti^{3+}OH + O_2 \rightarrow Ti^{4+}OH + O_2^{-\bullet}$$

The $O_2^{-\bullet}$ can generate hydroxyl radicals ($OH^{\bullet}$) *via* reaction with H^+.

$$O_2^{-\bullet} + H^+ \rightarrow HO_2^{\bullet}$$

$$HO_2^{\bullet} + H^+ + e^- \rightarrow H_2O_2$$

$$H_2O_2 + e^- \rightarrow OH^{\bullet} + OH^-$$

The suggested sources of H^+ are:

(1) The surface's hydroxyl groups of catalyst can act as an electron donor for photo-generated H^+.

(2) The hydroxyl groups of absorbed water vapor in the air on the surface of TiO_2@MCM-41.[36]

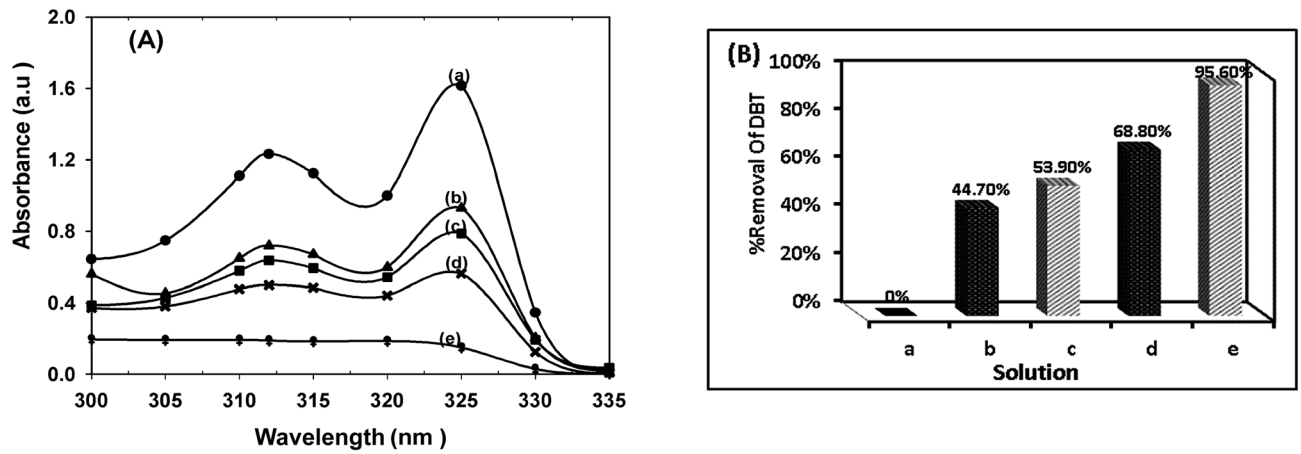

Fig. 12 (A) UV-Vis absorption spectra. (B) Percentage of DBT removal (a) standard solution of DBT (300 ppm), (b) DBT solution in the presence of CTM-41 (Si/Ti = 50) in dark for 45 min, (c) DBT solution in the presence of CTM-41 (Si/Ti = 5) in dark for 45 min, (d) DBT solution in the presence of CTM-41 (Si/Ti = 50) in dark for 45 min and light for 5 h, (e) DBT solution in the presence of CTM-41 (Si/Ti = 5) in dark for 45 min and light for 5 h, condition: under two lamps (300 W) irradiation, 10 mL DBT (300 ppm), 0.015 g catalyst, 60 °C.

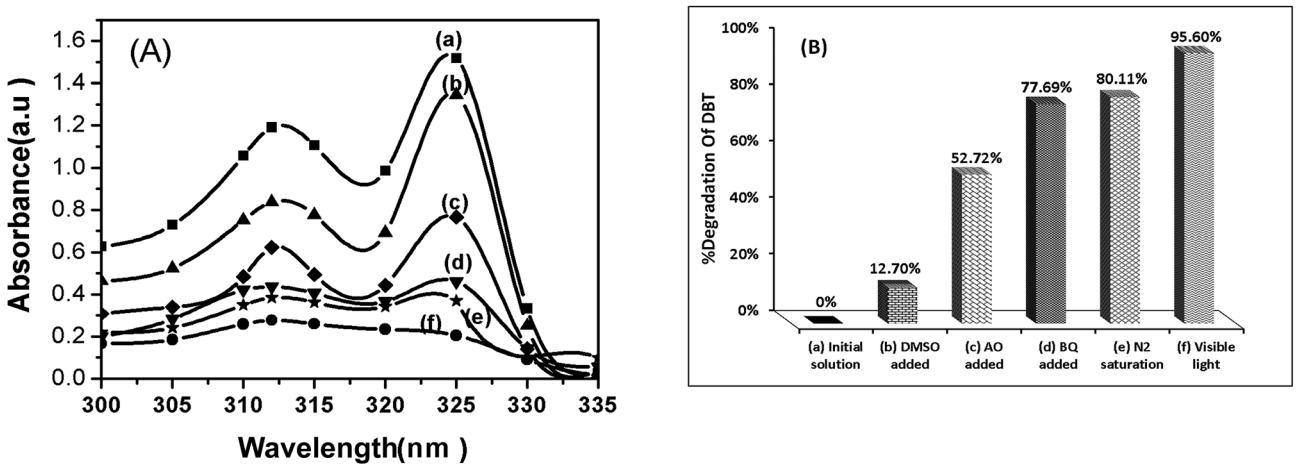

Fig. 13 The effect of radical scavengers on the photocatalytic degradation of DBT (A) UV-Vis absorption spectra. (B) Percentage of DBT degradation (a) standard solution of DBT (300 ppm), (b) with DMSO, (c) with AO, (d) with BQ, (f) without scavenger, condition: 0.015 g CTM-41 (Si/Ti = 5) under visible light irradiation for 5 h.

The photo-generated holes in C 2p states could not thermodynamically oxidize water or hydroxyl on catalyst surface. This is due to the lower potential of holes in the C 2p states (1.3 eV) than the standard redox potential of $OH^{\bullet}/H_2O$ (2.7 eV) as shown in Scheme 1. Therefore, the holes generated in the C 2p states acted as an oxidizing sites only for the adsorbed DBT,[46] not for the water or hydroxyl on the catalyst surface.

Another experiment was conducted to understand the effect of UV light irradiation. As shown in Fig. 14, the photo degradation efficiency of DBT decreased under UV light irradiation. To examine the cause for decreasing degradation of DBT, some experiments using radical scavengers were performed under UV irradiation. It can be seen that, under UV irradiation, the addition of AO as a scavenger for holes did not change the degradation of DBT. This result clearly suggests that holes (h^+) are not formed in C 2p states. This observation is reasonable because UV irradiation can only excite the electrons from valance band to the conduction band of TiO_2 but UV irradiation cannot excite the electrons from interband (C 2p level) to conduction band of TiO_2. The generated holes in valance band of TiO_2 can thermodynamically oxidize water and hydroxyl ions to produce hydroxyl radicals. The oxidation power of hydroxyl radicals (relative oxidation power = 2.05) is weaker than that of holes (relative oxidation power = 2.35).[47] Therefore, the degradation of DBT decreases under UV light. As shown in Fig. 14, it is found that hydroxyl radicals ($OH^{\bullet}$) and $O_2^{-\bullet}$ are the primary oxidants in the photocatalytic oxidation of DBT under UV light irradiation.

3.5 Possible DBT photocatalyzed degradation path

In order to describe the photodegradation pathway, the GC-MS analysis was performed on three solutions:

(1) Before photocatalytic degradation, the DBT solution (300 ppm) was analyzed by GC-MS. The GC chromatogram showed a peak at retention time (t_r) of 34.78 min. This peak was identified by GC-MS analysis and compared with standard samples. The retention time was corresponded to DBT.

(2) After photocatalytic degradation and catalyst separation by centrifuge, the GC-MS detected a large peak with the retention time of 24.96 min. This retention time was related to the production of biphenyl. Any peak containing a sulfur compound in the solution was not detected.

(3) To examine the adsorption of sulfur compounds on the surface, the catalyst separated from previous step was added to alcohol and stirred at about 30 °C. After desorption, the solution was collected and analyzed by GC-MS analysis. The sulfur species were not observed on the GC chromatogram.

Since the formation of biphenyl was observed from DBT solution after photocatalytic degradation and sulfur compounds were not detected, it is plausible to assume that the sulfur compounds were escaped as gas from the solution.

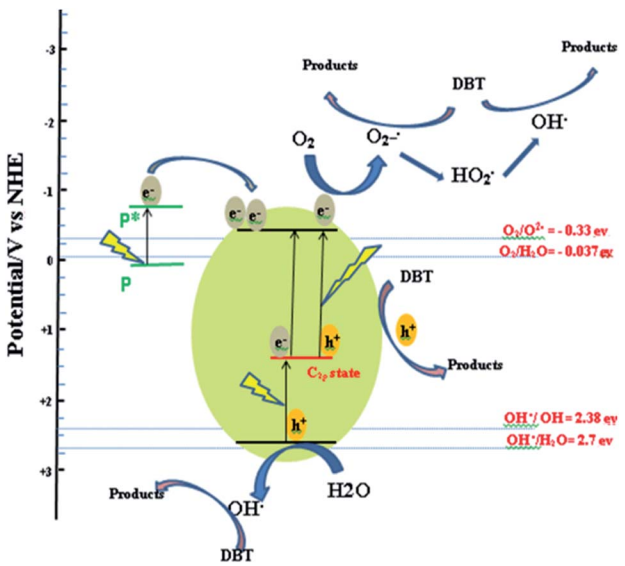

Scheme 1 Proposed mechanism for DBT degradation.

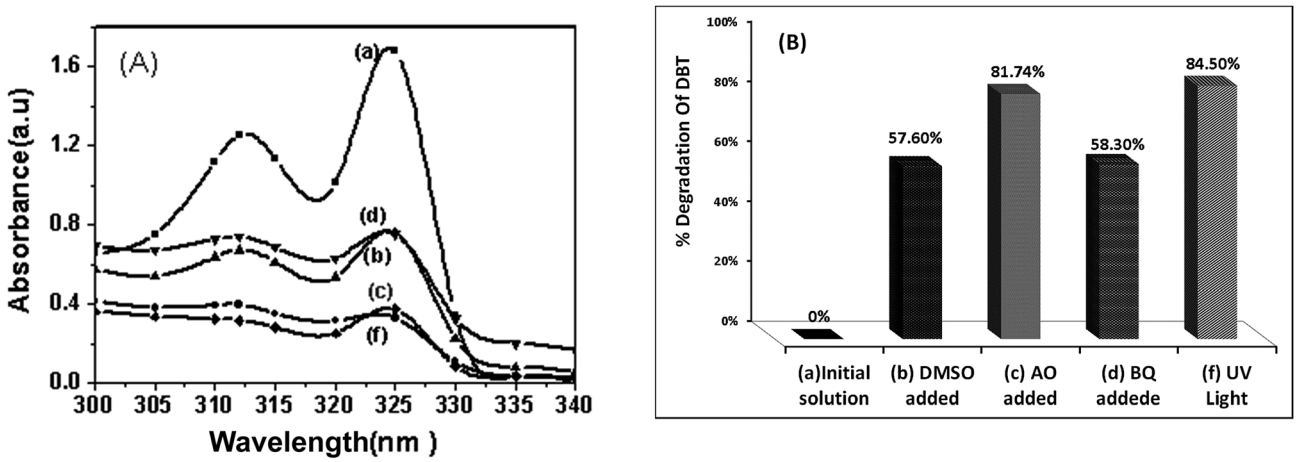

Fig. 14 The effect of radical scavengers on the photocatalytic degradation of DBT (A) UV-Vis absorption spectrum. (B) Percentage of DBT degradation (a) standard solution of DBT (300 ppm), (b) with DMSO, (c) with AO, (d) with BQ, (f) without scavenger, condition: 0.015 g CTM-41 (Si/Ti = 5) under UV light irradiation for 5 h.

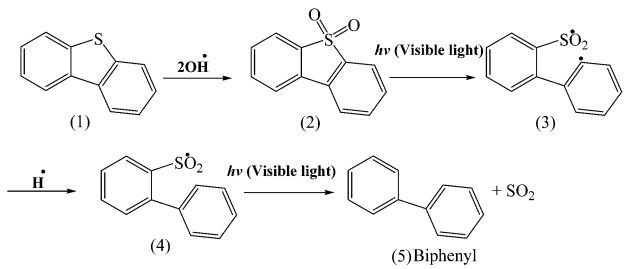

Scheme 2 Possible DBT photocatalyzed degradation path.

Based on the literature,[48,49] the DBT (**1**) can be converted to DBT sulfone (**2**) in the presence of $OH^{\bullet}$ and it is shown in Scheme 2. Shiraishi *et al.*[50] reported that when DBT sulfone was dissolved in 2-propanol and photo irradiated at $\lambda > 280$ nm by a high-pressure mercury lamp under air, the concentration of DBT sulfone decreases with time and the biphenyl concentration increased. In this work, as is shown in Scheme 2, first DBT (**1**) can convert to DBT sulfone (**2**) in the presence of $OH^{\bullet}$ and then DBT sulfone (**2**) is photoexcited by photo irradiation to form highly reactive 1,5-biradical (**3**) intermediate and then it is hydrogenated by OH groups of CTM-41 and further decomposed to form finally biphenyl (**5**).

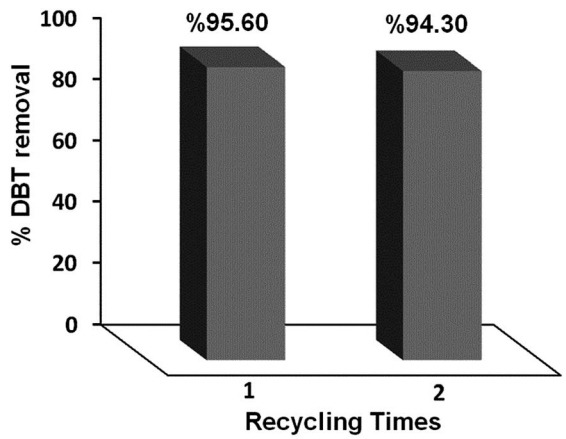

Fig. 15 Reusability of the photocatalyst.

3.6 Recycling of the catalyst

The recyclability of the CTM-41 (Si/Ti = 5) was performed by testing consecutive cycles of the photocatalytic process. Fig. 15 shows the percentage of desulfurization for this compound. It was observed that the catalytic system could be recycled at least two times with little decrease in DBT removal. After using, CTM-41 nanoparticles were separated from the solution with centrifuging and then used in another cycle.

4. Conclusions

In this work, carbon self-doped TiO_2@MCM-41 (CTM-41) nanoparticles were prepared. The CTM-41 nanoparticles with measured band gaps of 1.3 eV and 3.2 eV exhibited high photocatalytic activity. These band gaps were assigned to the isolated C 2p states of carbonate ions. According to the XPS and UV analyses, there are two forms of C in CTM-41: interstitial carbons (carbonate species) and coke-like structure which have both been considered as the source of the extended optical absorption in the visible range. The C-doped TM-41 samples exhibited an enhanced absorption in the visible light region. The results suggested that the photocatalytic degradation of DBT is 95.6% when CTM-41 (Si/Ti = 5) was used as a catalyst. The results of GC-MS analysis showed that DBT converts to biphenyl under visible light irradiation and mild conditions within 5 h. The photocatalytic degradation of DBT by CTM-41 could be done *via* direct reactions of DBT with holes and $OH^{\bullet}$ trapped on the surface.

Acknowledgements

The support of Ferdowsi University of Mashhad (Research and Technology) is appreciated for the Project (3/19276, 17/10/2011).

This work has also been supported by the "Iranian National Science Foundation: INSF" (no. 90001893).

References

1 C. Su, B. Y. Hong and C. M. Tseng, Sol–gel preparation and photocatalysis of titanium dioxide, *Catal. Today*, 2004, **96**(3), 119–126.

2 H. Tao, T. Nakazato and S. Sato, Energy-efficient ultra-deep desulfurization of kerosene based on selective photooxidation and adsorption, *Fuel*, 2009, **88**(10), 1961–1969.

3 A. Samokhvalov, *et al.*, Adsorption and desorption of dibenzothiophene on Ag-titania studied by the complementary temperature-programmed XPS and ESR, *Appl. Surf. Sci.*, 2011, **257**(8), 3226–3232.

4 A. H. M. Shahadat Hussain and B. J. Tatarchuk, Mechanism of hydrocarbon fuel desulfurization using Ag/TiO_2–Al_2O_3 adsorbent, *Fuel Process. Technol.*, 2014, **126**, 233–242.

5 A. Samokhvalov, *et al.*, Surface characterization of Ag/Titania adsorbents, *Appl. Surf. Sci.*, 2010, **256**(11), 3647–3652.

6 Y. Jia, G. Li and G. Ning, Efficient oxidative desulfurization (ODS) of model fuel with H_2O_2 catalyzed by MoO_3/γ-Al_2O_3 under mild and solvent free conditions, *Fuel Process. Technol.*, 2011, **92**(1), 106–111.

7 X. Zhou, *et al.*, Oxidative desulfurization of dibenzothiophene based on molecular oxygen and iron phthalocyanine, *Fuel Process. Technol.*, 2009, **90**(2), 317–323.

8 W. Guo, *et al.*, Oxidative desulfurization of diesel with TBHP/isobutyl aldehyde/air oxidation system, *Appl. Energy*, 2011, **88**(1), 175–179.

9 K. Castillo, *et al.*, Oxidation of dibenzothiophene to dibenzothiophene-sulfone using silica gel, *J. Catal.*, 2009, **268**(2), 329–334.

10 A. Al-Abduly and V. K. Sharma, Oxidation of benzothiophene, dibenzothiophene, and methyl-dibenzothiophene by ferrate(vi), *J. Hazard. Mater.*, 2014, **279**, 296–301.

11 A. Fujishima, T. N. Rao and D. A. Tryk, Titanium dioxide photocatalysis, *J. Photochem. Photobiol., C*, 2000, **1**(1), 1–21.

12 A. Fujishima and X. Zhang, Titanium dioxide photocatalysis: present situation and future approaches, *C. R. Chim.*, 2006, **9**(5–6), 750–760.

13 Y. Lan, Y. Lu and Z. Ren, Mini review on photocatalysis of titanium dioxide nanoparticles and their solar applications, *Nano Energy*, 2013, **2**(5), 1031–1045.

14 A. A. Belhekar, S. V. Awate and R. Anand, Photocatalytic activity of titania modified mesoporous silica for pollution control, *Catal. Commun.*, 2002, **3**(10), 453–458.

15 D. Zhao, *et al.*, Rapid and facile synthesis of Ti-MCM-48 mesoporous material and the photocatalytic performance for hydrogen evolution, *Int. J. Hydrogen Energy*, 2010, **35**(11), 5276–5283.

16 X. Yan, *et al.*, Preparation, Characterization and Photocatalytic Activity of TiO_2 Formed from a Mesoporous Precursor, *J. Porous Mater.*, 2004, **11**(3), 131–139.

17 H. Irie, Y. Watanabe and K. Hashimoto, Nitrogen-Concentration Dependence on Photocatalytic Activity of $TiO_{2-x}N_x$ Powders, *J. Phys. Chem. B*, 2003, **107**(23), 5483–5486.

18 J. H. Park, S. Kim and A. J. Bard, Novel Carbon-Doped TiO_2 Nanotube Arrays with High Aspect Ratios for Efficient Solar Water Splitting, *Nano Lett.*, 2005, **6**(1), 24–28.

19 C. Lettmann, *et al.*, Visible light photodegradation of 4-chlorophenol with a coke-containing titanium dioxide photocatalyst, *Appl. Catal., B*, 2001, **32**(4), 215–227.

20 R. Leary and A. Westwood, Carbonaceous nanomaterials for the enhancement of TiO_2 photocatalysis, *Carbon*, 2011, **49**(3), 741–772.

21 H. J. Yun, *et al.*, Facile preparation of high performance visible light sensitive photo-catalysts, *Appl. Catal., B*, 2010, **94**(3–4), 241–247.

22 S. Zheng and L. Gao, Synthesis and characterization of Pt, Au or Pd clusters deposited titania-modified mesoporous silicate MCM-41, *Mater. Chem. Phys.*, 2003, **78**(2), 512–517.

23 J. Robertson and T. J. Bandosz, Photooxidation of dibenzothiophene on TiO_2/hectorite thin films layered catalyst, *J. Colloid Interface Sci.*, 2006, **299**(1), 125–135.

24 S. Zheng, *et al.*, Preparation, characterization and photocatalytic properties of singly and doubly titania-modified mesoporous silicate MCM-41 by varying titanium precursors, *J. Mater. Chem.*, 2001, **11**(2), 578–583.

25 H. Yang, Y. Deng and C. Du, Synthesis and optical properties of mesoporous MCM-41 containing doped TiO_2 nanoparticles, *Colloids Surf., A*, 2009, **339**(1–3), 111–117.

26 K. Nishizawa, M. Okada and E. Watanabe, New preparation method of visible light responsive titanium dioxide photocatalytic films, *Mater. Sci. Appl.*, 2014, **5**, 112–123.

27 K. J. S. I. a. Y.-S. L. Palanivelu, Carbon Doping of TiO_2 for Visible Light Photo Catalysis – A review, *Carbon: Sci. Technol.*, 2007, **8**(3), 214–224.

28 S. Sakthivel and H. Kisch, Daylight Photocatalysis by Carbon-Modified Titanium Dioxide, *Angew. Chem., Int. Ed.*, 2003, **42**(40), 4908–4911.

29 C. Di Valentin and G. Pacchioni, Trends in non-metal doping of anatase TiO_2: B, C, N and F, *Catal. Today*, 2013, **206**, 12–18.

30 T.-H. Xu, *et al.*, Band structures of TiO(2) doped with N, C and B, *J. Zhejiang Univ., Sci., B*, 2006, **7**(4), 299–303.

31 Q. Chen, *et al.*, Enhanced visible photocatalytic activity of titania-silica photocatalysts: effect of carbon and silver doping, *Catal. Sci. Technol.*, 2012, **2**(6), 1213–1220.

32 B. J. Aronson, C. F. Blanford and A. Stein, Solution-Phase Grafting of Titanium Dioxide onto the Pore Surface of Mesoporous Silicates: Synthesis and Structural Characterization, *Chem. Mater.*, 1997, **9**(12), 2842–2851.

33 L. Guanglong, *et al.*, Synthesis, characterization and photocatalytic evaluation of visible light activated C-doped TiO_2 nanoparticles, *Nanotechnology*, 2012, **23**(29), 294003.

34 K. Madhusudan Reddy, S. V. Manorama and A. Ramachandra Reddy, Bandgap studies on anatase titanium dioxide nanoparticles, *Mater. Chem. Phys.*, 2003, **78**(1), 239–245.

35 V. Etacheri, *et al.*, A Highly Efficient $TiO_{2-x}C_x$ Nano-heterojunction Photocatalyst for Visible Light Induced Antibacterial Applications, *ACS Appl. Mater. Interfaces*, 2013, **5**(5), 1663–1672.
36 L.-B. Xiong, *et al.*, Ti^{3+} in the Surface of Titanium Dioxide: Generation, Properties and Photocatalytic Application, *J. Nanomater.*, 2012, **2012**, 13.
37 Y.-H. Hsien, *et al.*, Photodegradation of aromatic pollutants in water over TiO_2 supported on molecular sieves, *Appl. Catal., B*, 2001, **31**(4), 241–249.
38 X. Yang, *et al.*, Highly visible-light active C- and V-doped TiO_2 for degradation of acetaldehyde, *J. Catal.*, 2007, **252**(2), 296–302.
39 P. Wang, *et al.*, Carbon-sensitized and nitrogen-doped TiO_2 for photocatalytic degradation of sulfanilamide under visible-light irradiation, *Water Res.*, 2011, **45**(16), 5015–5026.
40 J. Yang, *et al.*, Visible-light photocatalysis in nitrogen–carbon-doped TiO_2 films obtained by heating TiO_2 gel–film in an ionized N_2 gas, *Thin Solid Films*, 2008, **516**(8), 1736–1742.
41 C. Di Valentin, G. Pacchioni and A. Selloni, Theory of Carbon Doping of Titanium Dioxide, *Chem. Mater.*, 2005, **17**(26), 6656–6665.
42 D. Chen, *et al.*, Carbon and Nitrogen Co-doped TiO_2 with Enhanced Visible-Light Photocatalytic Activity, *Ind. Eng. Chem. Res.*, 2007, **46**(9), 2741–2746.
43 G. Dai, *et al.*, A simple preparation of carbon and nitrogen co-doped nanoscaled TiO_2 with exposed {0 0 1} facets for enhanced visible-light photocatalytic activity, *J. Mol. Catal. A: Chem.*, 2013, **368–369**, 38–42.
44 S. Zheng, *et al.*, Synthesis, characterization and photocatalytic properties of titania-modified mesoporous silicate MCM-41, *J. Mater. Chem.*, 2000, **10**(3), 723–727.
45 G. A. Eimer, *et al.*, The influence of Ti-loading on the acid behavior and on the catalytic efficiency of mesoporous Ti-MCM-41 molecular sieves, *Catal. Today*, 2008, **133–135**, 639–646.
46 S. Banerjee, *et al.*, New Insights into the Mechanism of Visible Light Photocatalysis, *J. Phys. Chem. Lett.*, 2014, **5**(15), 2543–2554.
47 R. Munter, Advanced oxidation processes – current status and prospects, *Proc. Est. Acad. Sci., Chem.*, 2001, **50**(2), 59–80.
48 Z. Juan, *et al.*, Photocatalytic oxidation dibenzothiophene using TS-1, *Chem. Eng. J.*, 2010, **156**(3), 528–531.
49 R. Vargas and O. Núñez, The photocatalytic oxidation of dibenzothiophene (DBT), *J. Mol. Catal. A: Chem.*, 2008, **294**(1–2), 74–81.
50 Y. Shiraishi, *et al.*, Photochemical Production of Biphenyls from Oxidized Sulfur Compounds Obtained by Oxidative Desulfurization of Light Oils, *Energy Fuels*, 2002, **17**(1), 95–100.

